



# Simulation of concrete failure and fiber reinforced polymer fracture in confined columns with different cross sectional shape



Chiara Ceccato<sup>a</sup>, Marco Salvato<sup>b</sup>, Carlo Pellegrino<sup>a</sup>, Gianluca Cusatis<sup>c,\*</sup>

<sup>a</sup> Dept. of Civil, Arch. and Environ. Engineering, University of Padova, Via Marzolo 9, Padova, 35131, Italy

<sup>b</sup> William E. Boeing Department of Aeronautics & Astronautics, University of Washington, 311D Guggenheim Hall, Seattle, WA, 98195-2400, USA

<sup>c</sup> Dept. of Civil and Environmental Eng., Northwestern University, 2145 N Sheridan Rd, Evanston, IL, 60208-3109, USA

## ARTICLE INFO

### Article history:

Received 22 March 2016

Revised 17 July 2016

Available online 19 December 2016

### Keywords:

Fiber reinforced polymers

FRP Confined concrete

Lattice discrete particle model

Microplane model

Damage mechanics

## ABSTRACT

Fiber Reinforced Polymers (FRP) have been widely used in different civil engineering applications to enhance the performance of concrete structures through flexural, shear or compression strengthening. One of the most common and successful use of FRP sheets can be found in the confinement of existing concrete vertical elements which need rehabilitation or increased capacity in terms of strength and ductility. However, efficient design of FRP retrofitting urges the development of computational models capable of accurately capturing (a) the interaction between the axial strains and lateral expansion of concrete with the corresponding stress increase in the external jacket; and (b) the fracturing behavior of the FRP jacket. In this study, experimental data gathered from the literature and relevant to FRP-confined columns are simulated by adopting the Lattice Discrete Particle Model (LDPM) and the Spectral Microplane Model (SMPM), recently developed to simulate concrete failure and fracture of anisotropic materials, respectively. LDPM models the meso-scale interaction of coarse aggregate particles and it has been extensively calibrated and validated with comparison to a large variety to experimental data under both quasi-static and dynamic loading conditions but it has not been fully validated with reference to low confinement compressive stress states, relevant to the targeted application. This task, along with the calibration of SMPM for FRP, is pursued in the present research. The results show that, with the improvement of the existing LDPM constitutive equations to account for low confinement effects, LDPM and SMPM are able to predict the concrete material response governed by the nonlinear interaction of confined vertical members strengthened by means of externally bonded FRP composites.

© 2016 Elsevier Ltd. All rights reserved.

## 1. Introduction

External confinement of reinforced concrete columns by means of FRP composites has become a popular technique for the rehabilitation of existing structures and for the strengthening and ductility increase of structural members. The rapid emerging of this technology has led to several studies focusing on fully understanding the behavior of FRP-confined concrete: the literature abounds with axial compression test results on concrete specimens confined by FRP jackets and several models have been also formulated, aiming to predict the stress-strain response and the failure mechanisms during the loading history.

Various analytical formulations have been proposed in terms of stress-strain relationships, mostly for cylindrical columns charac-

terized by uniformly-confined concrete (Teng and Lam 2004), including design-oriented model, in the form of closed-form expressions deduced from test data on FRP-confined concrete specimens (Lam and Teng 2003; Rousakis et al. 2012; Ozbakkaloglu and Lim 2013), and analysis-oriented models, in the form of an incremental iterative formulation explicitly accounting for the concrete core-FRP interaction (Jiang and Teng 2007; Binici 2005; Teng et al. 2007; Moran and Pantelides 2012). The behavior of non uniformly confined concrete, typical of square and rectangular sections, can also be approximately taken into account (Pellegrino and Modena 2010; Harajli 2006; Maalej et al. 2003) through aspect ratio factors or by ad-hoc modifications of the original formulations, but the stress variations over the section are difficult to be captured and understood (Yu et al. 2010a).

In addition, advanced numerical models have been used to capture the interaction mechanisms between FRP and concrete in further details. These simulations need a sound constitutive model for concrete, in order for the results to be accurate and

\* Corresponding author.

E-mail addresses: [chiara.ceccato@dicea.unipd.it](mailto:chiara.ceccato@dicea.unipd.it) (C. Ceccato), [salvato@aa.washington.edu](mailto:salvato@aa.washington.edu) (M. Salvato), [carlo.pellegrino@unipd.it](mailto:carlo.pellegrino@unipd.it) (C. Pellegrino), [g-cusatis@northwestern.edu](mailto:g-cusatis@northwestern.edu) (G. Cusatis).

different options have been explored for this scope. Several 3D FE implementations use plasticity models, mostly based on Drucker–Prager Plasticity, with different definitions of yield criterion, hardening rule and flow rule to take confinement effects into account (e.g. Rousakis et al. 2007; Karabinis and Rousakis 2002; Fam and Rizkalla 2001; Mirmiran et al. 2000). Amongst them, the method developed by Yu et al. (2010a) makes use of a hardening/softening rule which is assumed to depend on the confining pressure and of a confinement-dependent non-associated flow rule. Other 3D formulations are based on plastic-damage models (Yu et al. 2010b), able to simulate reductions in elastic stiffness of concrete and capture non-uniformly distributed stresses. More recently, also the microplane model (Bažant et al. 2000; Di Luzio 2007), considered capable of realistically simulating behavior of concrete under dominant tension, compression and complex non-proportional loading histories, has been used (Gambarelli et al. 2014). 1D models have also been proposed as simplified numerical tools to simulate cycling loading, using for instance elastic-damage models (Desprez et al. 2013) and using fibers models allowing non linearly distributed inelasticity (Teng et al. 2015a).

Most of these FE macroscopic models present limitations due to the simplifications in the constitutive laws for concrete softening response and often the good agreement between experimental data and numerical models is not general but oriented to specific applications and derived from limited empirical evidences, as highlighted, amongst others, by Yu et al. (2010a), Yu et al. (2010b), Gambarelli et al. (2014). The precise and accurate material dilatation properties during the microcracking evolution and fracture propagations, in particular, is crucial for capturing the post-peak response of FRP confined concrete (Lam and Teng 2003). The confining action of FRP jackets develops progressively during the vertical member compression process, increasing gradually and continuously in response to the lateral strain of concrete, which is, in turn, dependent on the axial strain. The mechanisms activated during the fracturing process of the material are complex and not easy to capture in a simplified macroscopic model. An interesting summary of the challenges faced by the research community on the development of a realistic numerical model for FRP confined concrete in particular and a constitutive relation for concrete in general is given by Yu-Fei Wu (Wu 2015): in his opinion, a large number of empirical models have been developed for different applications, most of which, though, are limited in their applicability, because they are mostly formulated at the macroscopic scale and are phenomenologically based.

For these reasons, in this work, a recently developed meso-scale model for concrete, called the Lattice Discrete Particle Model (LDPM) (Cusatis et al. 2011b), has been explored for the simulation of FRP-confined response of concrete columns. LDPM simulates concrete materials through the meso-scale interaction of coarse aggregate particles and it has been extensively calibrated and validated with comparison to a large variety of experimental data under both quasi-static and dynamic loading conditions. One of the most important aspect of LDPM is its unique capability of predicting macroscopic stress-strain curves and failure modes in compression simply through tensile and shearing softening at the meso-scale and without postulating the existence of softening in compression (Cusatis et al. 2011a; Schaufert and Cusatis 2011; Schaufert et al. 2012; Alnagar et al. 2013; Smith et al. 2015). LDPM, though, has not been fully validated with reference to low confinement compressive stress states, relevant to the targeted application and this is one of the aims of the present research.

As far as the FRP modeling is concerned, different methods have been explored, mostly based on two main approaches: (1) shell elements with orthotropic behavior and (2) isoparametric brick elements with an isotropic material representing the matrix and embedded reinforcement representing the fibers. Most of the mod-

els developed for FRP-confined concrete are based on type (1) approach (e.g. Shahawy et al. 2000; Karabinis et al. 2008; Koksal et al. 2009; Elsanadedy et al. 2012; Jiang and Wu 2012; Teng et al. 2015b), with linear elastic material generally acting only in the hoop direction and failing brittlely when the hoop tensile rupture strain is reached. They can provide sufficiently accurate predictions during the loading history of FRP-confined columns, but they are not accurate enough to capture the global failure condition, especially in case of non circular sections. For this reason, additional variables influencing the behavior of FRP jackets (such as curvature, resin type, thickness of the plies etc) have been taken into account by some researchers (see Rousakis et al. 2008). Type (2) approach has been rarely used for confinement applications because of the higher computational effort. One example can be found in Gambarelli et al. (2014).

## 2. Material Models: an overview

### 2.1. Lattice Discrete Particle Model (LDPM) for concrete

LDPM simulates the failure behavior of concrete by modeling aggregate interaction within the material meso-structure. As accurately described in Cusatis et al. (2011b), the procedure defining the material internal structure is based on the definition of the number and size of the aggregates pieces, their position, their interconnections and also the surfaces through which forces are transmitted between them. The following steps summarize how the material internal structure is built:

1. The coarse aggregate pieces (particles), assumed to be spherical, are introduced into the concrete volume by a try-and-reject random procedure. The number and dimension of particles to be placed inside the specimen volume  $V$  are determined from a set of mix-design parameters, namely cement content  $c$ , water-to-cement ratio  $w/c$ , aggregate-to-cement ratio  $a/c$ , maximum aggregate size  $d_a$ , minimum aggregate size  $d_0$  (governing the model resolution), and Fuller coefficient  $\eta_f$ . The aggregate volume fraction is then computed and a consistent granulometric distribution of particles size, spanning from  $d_0$  to  $d_a$ , is randomly generated according to the Fuller curve.
2. Over the external surfaces, zero-radius aggregate pieces (nodes) are distributed so that the surface discretization resolution is comparable to the one inside the specimen, firstly placing the vertex nodes, then the edge and surface nodes. The particles are finally located inside the specimen in order to create a statistically isotropic random mesostructure, using the procedure described in Cusatis et al. (2011b).
3. A three-dimensional domain tessellation, based on the Delaunay tetrahedralization of the generated aggregate centers, creates a system of cells interacting through triangular facets, which can be represented, in a three-dimensional setting, as shown in Fig. 1. The tessellation of a tetrahedron is shown in Fig. 1a: in general, it can be obtained by a set of triangles, defined by a point on the tetrahedron edge (edge-points  $E_{ij}$ ), a point on the tetrahedron face (face-points  $F_i$  and a point inside the tetrahedron (tet-point  $T_i$ ). A polyhedral cell containing the particle is created by the collection of facets associated with each particle (Fig. 1b). The definition of these surfaces where the interaction forces are exchanged, corresponds to damage localization zones, consistently with the fracture initiating and propagating in the mortar paste.

The governing equations are derived from the basic unit of the model, which is a four-particle tetrahedron, to be subdivided into four subdomains, each associated to one particle, the portion of the three tetrahedron edges attached to the node and the six triangular tessellation facets attached to those edges. The displacement

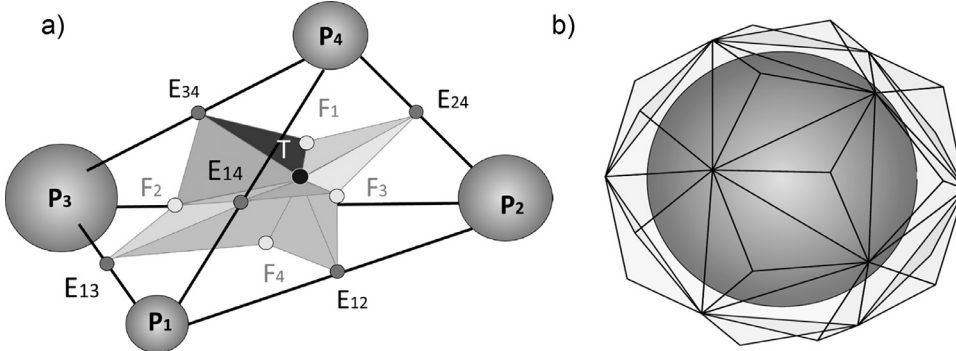


**Fig. 1.** (a) Tessellation of a typical LDPM tetrahedron connecting four adjacent particles; (b) Polyhedral cell.

field is defined according to the rigid-body kinematics for every subdomain. Consequently, a displacement jump  $[[\mathbf{u}_{Ck}]]$  can be defined at the centroid of each tetrahedron facet. The facet strain vector can be defined as the displacement jump at the contact point divided by the inter-particle distance. The strain vector is decomposed into its normal and shear components. Note that the projection of the facets are used instead of the facets themselves for the decomposition, in order to ensure that the shear interaction between adjacent particles does not depend on the shear orientation (Cusatis et al. 2011b). If the unit vectors  $\mathbf{n}$ ,  $\mathbf{l}$ , and  $\mathbf{m}$  define a local system of reference on the projected facets, one can write:

$$\varepsilon_{Nk} = \frac{\mathbf{n}_k^T [[\mathbf{u}_{Ck}]]}{\ell_e}; \quad \varepsilon_{Mk} = \frac{\mathbf{m}_k^T [[\mathbf{u}_{Ck}]]}{\ell_e}; \quad \varepsilon_{Lk} = \frac{\mathbf{l}_k^T [[\mathbf{u}_{Ck}]]}{\ell_e}. \quad (1)$$

The corresponding normal and shear stress are calculated through meso-scale constitutive laws and the equilibrium is finally imposed through the Principle of Virtual Work (PVW).

### 2.1.1. Elastic behavior

As described in details in Cusatis et al. (2011b), the elastic behavior for LDPM is formulated assuming that stresses and corresponding strains are proportional:

$$\sigma_N = E_N \varepsilon_N; \quad \sigma_M = E_T \varepsilon_L; \quad \sigma_L = E_T \varepsilon_L; \quad (2)$$

where  $E_N = E_0$  ( $E_0$ , effective normal modulus),  $E_T = \alpha E_0$  ( $\alpha$ , shear-normal coupling parameter).  $E_0$  and  $\alpha$  are considered as elastic material properties to be identified from experimental tests. The relationship between these meso-scale LDPM parameters and the traditional macroscopic parameters  $E$  (Young Modulus) and  $\nu$  (Poisson ratio) can be obtained considering an infinite number of facets surrounding the aggregate piece (see for example Bažant and Prat 1988; Carol and Bažant 1997):  $E_0 = E/(1-2\nu)$  corresponding to  $E = E_0(2+3\alpha)/(4+\alpha)$  and  $\alpha = (1-4\nu)/(1+\nu)$  corresponding to  $\nu = (1-\alpha)/(4+\alpha)$ .

### 2.1.2. Fracturing behavior

The fracturing behavior, characterized by tensile normal strains  $\varepsilon_N > 0$ , can be formulated with a relationship between the effective strain,  $\varepsilon = \sqrt{\varepsilon_N^2 + \alpha(\varepsilon_L^2 + \varepsilon_M^2)}$ , and the effective stress,  $\sigma = \sqrt{\sigma_N^2 + (\sigma_L^2 + \sigma_M^2)/\alpha}$ . The effective stress is assumed to be incrementally elastic  $\dot{\sigma} = E_0 \dot{\varepsilon}$  and its values can span from 0 to a limit strain dependent boundary  $\sigma_{bt}(\varepsilon, \omega)$  defined as

$$\sigma_{bt}(\varepsilon, \omega) = \sigma_0(\omega) \exp \left[ -H_0(\omega) \frac{\langle \varepsilon_{max} - \varepsilon_0(\omega) \rangle}{\sigma_0(\omega)} \right] \quad (3)$$

The variable  $\omega$  represents the degree of interaction between shear and normal stress:  $\tan \omega = \varepsilon_N / \sqrt{\alpha} \varepsilon_T = \sigma_N \sqrt{\alpha} / \sigma_T$ , where  $\varepsilon_T$  is the total shear strain,  $\sigma_T$  is the total shear stress and  $\varepsilon_0(\omega) = \sigma_0(\omega) / E_0$ .

The function  $\sigma_0(\omega)$ , strength limit for the effective stress, is defined as:

$$\sigma_0(\omega) = \sigma_t \frac{-\sin \omega + \sqrt{\sin^2 \omega + 4\alpha \cos^2 \omega (\sigma_t^2 / \sigma_s^2)}}{2\alpha \cos^2 \omega (\sigma_t^2 / \sigma_s^2)} \quad (4)$$

being  $\sigma_t$  the tensile strength and  $\sigma_s$  the shear strength.

When the maximum elastic strain reaches the elastic limit, the boundary  $\sigma_{bt}$  starts to decay. The softening modulus, governing the decay rate, is defined as:

$$H_0(\omega) = H_t \left( \frac{2\omega}{\pi} \right)^{n_t} = \frac{2E_0}{\ell_t / \ell - 1} \left( \frac{2\omega}{\pi} \right)^{n_t} \quad (5)$$

where  $\ell_t = 2E_0 G_t / \sigma_t^2$ ,  $G_t$  is the meso-scale fracture energy and  $\ell$  is the interparticle distance coinciding with the length of the tetrahedron edge associated with the current facet. For further details, the reader is referred to Cusatis et al. (2011b).

### 2.1.3. Compressive behavior

In order to simulate pore collapse and material compaction, the LDPM constitutive law in compression is based on a strain-hardening normal boundary  $\sigma_{bc}$  limiting the compressive normal stress component at the facet level.  $\sigma_{bc}$  is assumed to be a function of the volumetric strain  $\varepsilon_V = (V - V_0)/V_0$ , being  $V$  and  $V_0$  the current and initial volume of the tetrahedron, and deviatoric strain  $\varepsilon_D = \varepsilon_N - \varepsilon_V$ .

For a given deviatoric-to-volumetric strain ratio  $r_{DV} = \varepsilon_D / \varepsilon_V$ , the compressive boundary can be formulated as:

$$\sigma_{bc}(\varepsilon_D, \varepsilon_V) = \begin{cases} \sigma_{c0} & \text{for } -\varepsilon_{DV} \leq 0 \\ \sigma_{c0} + (-\varepsilon_{DV} - \varepsilon_{c0}) H_c(r_{DV}) & \text{for } 0 \leq -\varepsilon_{DV} \leq \varepsilon_{c1} \\ \sigma_{c1}(r_{DV}) \exp [(-\varepsilon_{DV} - \varepsilon_{c1}) H_c(r_{DV}) / \sigma_{c1}(r_{DV})] & \text{otherwise} \end{cases} \quad (6)$$

where  $\varepsilon_{DV} = \varepsilon_V + \beta \varepsilon_D$  ( $\beta$  is a material parameter),  $\varepsilon_{c0} = \sigma_{c0} / E_0$  is the compaction strain at the beginning of the pore collapse,  $H_c(r_{DV})$  the initial hardening modulus,  $\varepsilon_{c1} = \kappa_{c0} \varepsilon_{c0}$  the compaction strain at which rehardening begins,  $\kappa_{c0}$  the material parameter governing the rehardening and  $\sigma_{c1}(r_{DV}) = \sigma_{c0} + (\varepsilon_{c1} - \varepsilon_{c0}) H_c(r_{DV})$ .

In Cusatis et al. (2011b), the slope of the initial hardening modulus is assumed to go to zero for increasing values of  $r_{DV}$ :

$$H_c(r_{DV}) = \frac{H_{c0}}{1 + \kappa_{c2} (r_{DV} - \kappa_{c1})} \quad (7)$$

where  $H_{c0}$ ,  $\kappa_{c1}$ ,  $\kappa_{c2}$  are assumed to be material parameters.

### 2.1.4. Frictional behavior

In case of compression, the shear strength of concrete increases because of frictional effects. This phenomenon can be simulated through incremental plasticity, with incremental stresses defined

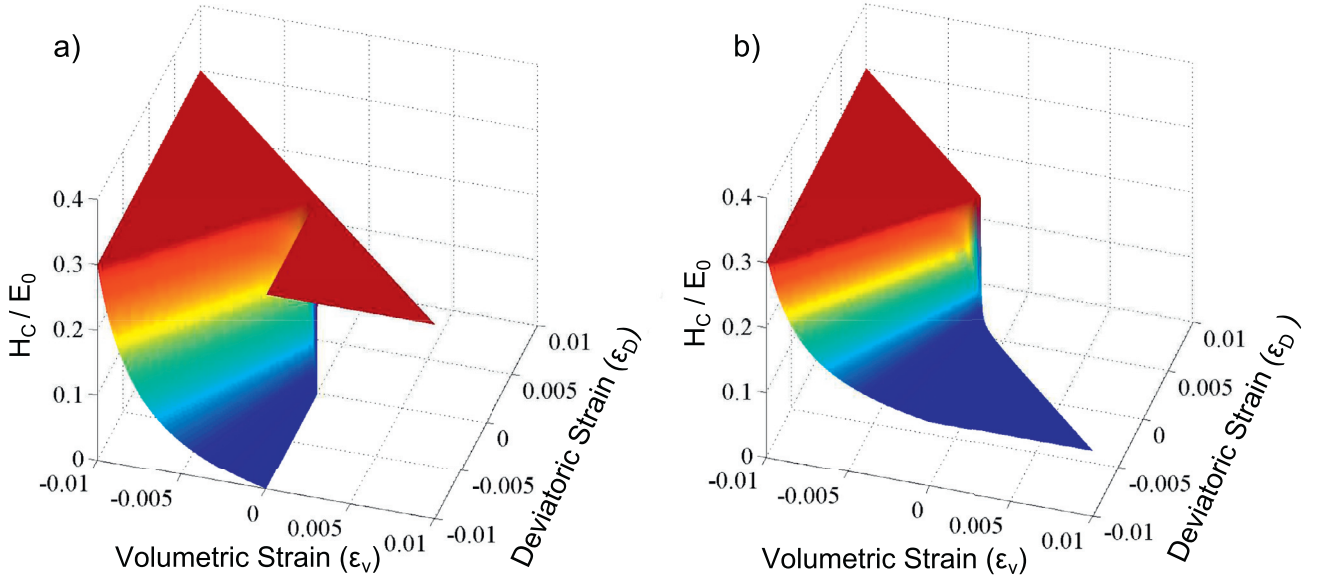


**Fig. 2.** 3D plot of the adimensionalized hardening modulus function ( $H_c/E_0$ ) (a) original formulation and (b) new formulation.

as  $\dot{\sigma}_M = E_T(\dot{\varepsilon}_M - \dot{\varepsilon}_M^p)$   $\dot{\sigma}_L = E_T(\dot{\varepsilon}_L - \dot{\varepsilon}_L^p)$ . The plastic potential can be expressed as  $\varphi = \sqrt{\sigma_M^2 + \sigma_L^2} - \sigma_{bs}(\sigma_N)$ , where

$$\sigma_{bs} = \sigma_s + (\mu_0 - \mu_\infty)\sigma_{N0} - \mu_\infty\sigma_N - (\mu_0 - \mu_\infty)\sigma_{N0}\exp(\sigma_N/\sigma_{N0}) \quad (8)$$

being  $\sigma_s$  the cohesion,  $\mu_0$  and  $\mu_\infty$  the initial and final friction coefficients and  $\sigma_{N0}$  the normal stress at which the friction coefficient transitions from  $\mu_0$  to  $\mu_\infty$ . The plastic strain increments are assumed to obey the normality rule  $\dot{\varepsilon}_M = \lambda \frac{\partial \varphi}{\partial \sigma_N}$  and  $\dot{\varepsilon}_L = \lambda \frac{\partial \varphi}{\partial \sigma_L}$ .

The current LDPM formulation is implemented in MARS, a multi-purpose computational code for the explicit dynamic simulation of structural performance (Pelessone 2015).

## 2.2. Modification of LDPM constitutive law in compression

Preliminary simulations revealed that the constitutive law in compression governs the inelastic response of FRP-reinforced concrete for large enough confinement. The original LDPM formulation, described in Section 2.1 and with more details in Cusatis et al. (2011b), was conceived initially to describe the strain hardening plasticity under high compressive confinement, with micro and meso-scale pore collapse under load followed by a densification due to the contact between completely collapsed pores.

The aforementioned constitutive law, though, shows its limits when applied to the low confinement stress states, which are typical of the FRP confinement problems: the formulated hardening modulus function  $H_c$  (see Eq. (7)) is not suitable for negative deviatoric-to-volumetric strain ratios, generally experienced by the material in these cases. In fact, when transitioning from negative to positive volumetric strains at constant deviatoric strain, the original formulation exhibits a discontinuity in the definition of  $H_c$  (Fig. 2a) such that the material appears to gain strength during the dilation process. This response is unrealistic and in contrast with typical experimental evidence. Since for  $\varepsilon_N > 0$  a different set of equations governs the response (see Section 2.1.2), in Fig. 2a  $H_c$  is plotted only for  $\varepsilon_N = \varepsilon_D + \varepsilon_V < 0$ .

Fig. 3 illustrates the typical behavior of FRP confined concrete columns compared to unconfined concrete columns, from experimental data by Wang and Wu (2008). The deviatoric strain vs. axial strain curves, where strains are computed as defined in Section 2.1, are regularly increasing for both confined and unconfined concrete.

On the contrary, while the volumetric strain vs. axial strain curves show a different behavior: after an initial compaction, the material expands as long as the external confinement is able to contrast it by constraining the lateral deformations. The stiffer the wrapping, the sooner the material can reverse the dilation trend and experience re-compaction. Moreover, if the confining stress is high, the material does not experience dilation at all.

The same behavior is shown in Fig. 4, where the axial stress is plotted against the volumetric strain for both actively and passively confined concrete specimens. As described in detail in Teng and Lam (2004), for active confinement, the change from compaction to dilation occurs at different stress levels depending on the confining pressure, and thereafter the dilation tendency remains up to failure. For passive confinement, instead, dilatation can be taken over again by compaction, therefore the accurate description of the hardening function around the zero volumetric strains is particularly crucial in this case.

To overcome the discussed limitations of the LDPM formulation, a new definition for the hardening modulus is proposed in this work with Eq. (9). The hardening modulus  $H_c$  is formulated to allow a continuous behavior for compaction to dilation transitions:

$$H_c = \frac{H_{c0} - H_{c1}}{1 + \kappa_{c2}(r_{DV} - \kappa_{c1})} + H_{c1}; \quad (9a)$$

$$r_{DV} = \begin{cases} -\frac{|\varepsilon_D|}{\varepsilon_V - \varepsilon_{V0}} & \text{for } \varepsilon_V \leq 0 \\ \frac{|\varepsilon_D|}{\varepsilon_{V0}} & \text{for } \varepsilon_V > 0 \end{cases} \quad (9b)$$

>with  $\varepsilon_{V0} = \kappa_{c3} \cdot \varepsilon_0 = 0.1 \cdot \varepsilon_0$  ( $\kappa_{c3} = 0.1$ ) and  $H_{c1}$  to be calibrated with experimental data.

This new function permits a smooth and coherent transition from contraction to expansion and viceversa: the hardening modulus decreases continuously for increasing volumetric strain and constant deviatoric strain. Similarly, for constant volumetric strain,  $H_c$  decreases for increasing (in absolute value) deviatoric strains.

### 2.2.1. Calibration

Two sets of parameters control LDPM response. The first set, relevant to the geometrical definition of the mesostructure, is de-

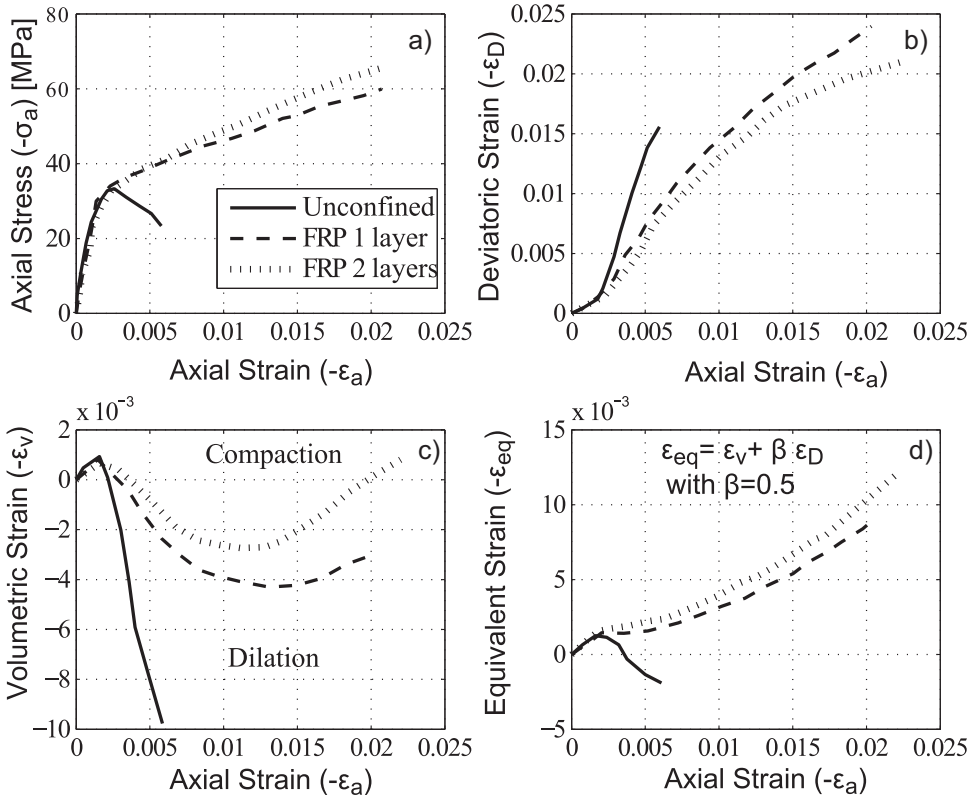


**Fig. 3.** (a) Axial stress vs. axial strain curves, (b) deviatoric strain vs. axial strain curves, (c) volumetric strain vs. axial strain curves and (d) equivalent strain vs. axial strain curves for unconfined and FRP-confined concrete.

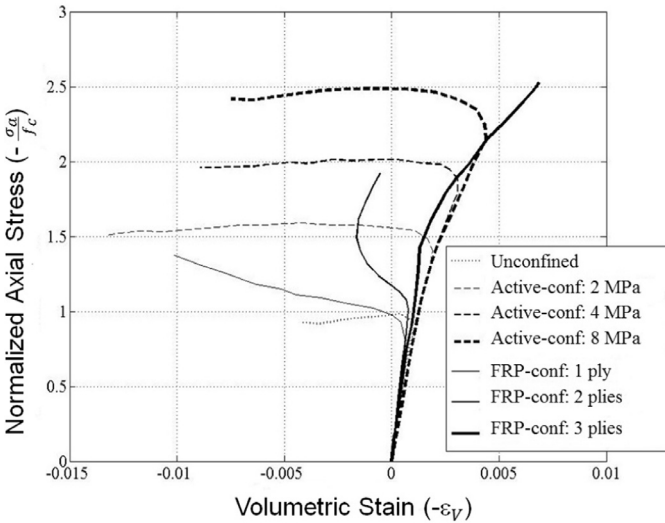


**Fig. 4.** Stress vs. volumetric strain responses of confined concrete.

scribed in paragraph 2.1. The second set, relevant to the constitutive laws at the facet level, includes: normal elastic modulus  $E_0$ , shear-normal coupling parameter  $\alpha$ , tensile strength  $\sigma_t$ , characteristic length  $\ell_t$ , softening exponent  $n_t$ , shear strength  $\sigma_s$ , yielding compressive stress  $\sigma_{c0}$ , initial hardening modulus  $H_{c0}$ , transitional strain ratio  $\kappa_{c0}$ , densified normal modulus  $E_d$ , initial internal friction coefficient  $\mu_0$ , internal asymptotic friction coefficient  $\mu_\infty$ , internal asymptotic friction coefficient  $\sigma_{N0}$ , deviatoric-to-volumetric strain ratio  $\kappa_{c1}$ , deviatoric damage parameter  $\kappa_{c2}$ , unloading/reloading parameter  $\kappa_{c2}$ . Calibration of LDPM parameters can be obtained through the best fitting of the complete load

displacement curves relevant to five different experimental tests: (1) hydrostatic compression; (2) unconfined compression; (3) fracture test (with unloading/reloading cycles if cycling loading is of interest and the parameter  $k_t$  needs to be calibrated); (4) triaxial compression at low-confinement; and (5) triaxial compression at high-confinement. For more details about the calibration process, one can refer to Cusatis et al. (2011a).

### 2.3. Spectral stiffness microplane model for composite laminates

For the simulation of the columns wrapping, the FRP jacketing is modeled in this study by means of the Spectral Stiffness Microplane Model (Cusatis et al. 2008; Salviato et al. 2016), which is a general constitutive model for unidirectional and textile composite laminates able to simulate orthotropic stiffness, pre-peak non linearity, failure envelopes, post-peak softening and fracture.

#### 2.3.1. Theoretical background on microplane model and spectral stiffness theorem

The Spectral Stiffness Microplane Model is based on the framework of the original kinematically constrained microplane model (Bažant and Oh 1985; Bažant et al. 2000; Caner and Bažant 2012; Bažant and Di Luzio 2004; Di Luzio and Cusatis 2013; Cusatis and Zhou 2014) which rests on two basic ideas: (1) the constitutive relations describe micro structural phenomena not in terms of stress and strain tensors, but in terms of the stress and strain vectors acting on planes of all possible orientations at a given point of the continuum; and (2) a variational principle is used to relate the microplane vectors to the continuum tensors.

According to Cusatis et al. (2008), the Spectral Stiffness Decomposition theorem (Rychlewski 1995; Theocaris and Sokolis 1998; 1999; 2000) is used to extend the microplane framework to account for material anisotropy. The stiffness matrix of the composite

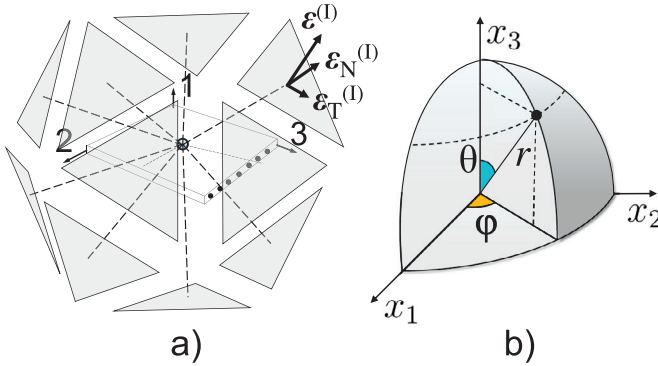


**Fig. 5.** Schematic representation of (a) Representative Unit Cell for FRP; (b) local spherical coordinate system.

$\mathbf{C}$  is decomposed as follows:

$$\mathbf{C} = \sum_I \lambda^{(I)} \mathbf{C}^{(I)} \quad (10)$$

where  $I = 1, 2, \dots, 6$ ,  $\lambda^{(I)}$  are the eigenvalues of the stiffness matrix and  $\mathbf{C}^{(I)} = \sum_n \Phi_{In} \Phi_{In}^T$  are a set of second-order tensors constructed from the elastic eigenvectors  $\Phi_I$ . The  $I$ -th eigenvector  $\Phi_I$  has multiplicity  $n$  and is normalized such that  $\Phi_I^T \mathbf{C}^{(I)} \Phi_I = \lambda^{(I)}$ .

An important characteristic of the elastic eigenmatrices  $\mathbf{C}^{(I)}$  is that they provide a way to decompose the stress and strain tensors into energetically orthogonal modes. These are called here *eigenstresses* and *eigenstrains* and are defined as:

$$\sigma_I = \mathbf{C}^{(I)} \sigma \quad \text{and} \quad \epsilon_I = \mathbf{C}^{(I)} \epsilon \quad (11)$$

It is easy to show that  $\sigma = \sum_I \sigma_I$  and  $\epsilon = \sum_I \epsilon_I$  whereas the relation between eigenstresses and eigenstrains can be found introducing the related elastic eigenvalues:  $\sigma_I = \lambda^{(I)} \epsilon_I$ . By the spectral decomposition of the strain tensor and a separate projection of each eigenstrain, each microplane vector can be decomposed into microplane eigenstrain vectors as:

$$\epsilon_P = \sum_I \epsilon_P^{(I)} \quad \text{where} \quad \begin{cases} \epsilon_P^{(I)} = \mathbf{P} \epsilon^{(I)} = \mathbf{P} \mathbf{C}^{(I)} \epsilon \\ \mathbf{P}^{(I)} = \mathbf{P} \mathbf{C}^{(I)} \end{cases} \quad (12)$$

where  $N$  = number of independent eigenmodes and:

$$\mathbf{P} = \begin{bmatrix} N_{11} & N_{22} & N_{33} & \sqrt{2}N_{23} & \sqrt{2}N_{13} & \sqrt{2}N_{12} \\ M_{11} & M_{22} & M_{33} & \sqrt{2}M_{23} & \sqrt{2}M_{13} & \sqrt{2}M_{12} \\ L_{11} & L_{22} & L_{33} & \sqrt{2}L_{23} & \sqrt{2}L_{13} & \sqrt{2}L_{12} \end{bmatrix} \quad (13)$$

is a  $3 \times 6$  matrix relating the macroscopic strain tensor to the microplane strain as a function of the plane orientation, where  $\epsilon$  and  $\sigma$  are expressed in Kelvin notation,  $N_{ij} = n_i n_j$ ,  $M_{ij} = (m_i n_j + m_j n_i)/2$  and  $L_{ij} = (l_i n_j + l_j n_i)/2$ , where  $n_i$ ,  $m_i$  and  $l_i$  define a local Cartesian reference system on the generic microplane with  $n_i$  being the  $i$ th component of the normal unit vectors and  $l_i$ ,  $m_i$  the  $i$ th components of two mutually orthogonal unit vectors also orthogonal to  $n_i$  (Fig. 5a). With reference to the spherical coordinate system represented in Fig. 5b, the foregoing components can be expressed as a function of the spherical angles  $\theta$  and  $\varphi$ :  $n_1 = \sin \theta \cos \varphi$ ,  $n_2 = \sin \theta \sin \varphi$ ,  $n_3 = \cos \theta$  while one can choose  $m_1 = \cos \theta \cos \varphi$ ,  $m_2 = \cos \theta \sin \varphi$ ,  $m_3 = -\sin \theta$  which gives, for orthogonality,  $l_1 = -\sin \varphi$ ,  $l_2 = \cos \varphi$  and  $l_3 = 0$  (Cusatis et al. 2008). In this way, different constitutive laws describing the material behavior at the microplane level can be related to each eigenmode, allowing not only the description of the material anisotropy but also to address the different damaging mechanisms related to different loading conditions. Accordingly, from the microplane eigenstrains, the microplane eigenstresses  $\sigma_P^{(I)}$  can be defined through

specific constitutive laws:  $\sigma_P^{(I)} = f(\epsilon_{P1}, \epsilon_{P2}, \dots) \epsilon_P^{(I)}$  and the macroscopic stress tensor can be computed through the principle of virtual work (Cusatis et al. 2008):

$$\sigma = \frac{3}{2\pi} \int_{\Omega} \mathbf{P}^T \sum_I \sigma_P^{(I)} d\Omega \quad (14)$$

where  $\Omega$  is the surface of a unit hemi-sphere representing all the possible microplane orientations.

#### Constitutive laws: elastic behavior

The elastic behavior is formulated by assuming that normal and shear eigenstresses on the microplanes are proportional to the corresponding eigenstrains:

$$\sigma_N^{(I)} = \lambda^{(I)} \epsilon_N^{(I)}, \quad \sigma_M^{(I)} = \lambda^{(I)} \epsilon_M^{(I)}, \quad \sigma_L^{(I)} = \lambda^{(I)} \epsilon_L^{(I)} \quad (15)$$

where  $\lambda^{(I)}$  =  $I$ th elastic eigenvalue.

#### Constitutive laws: inelastic behavior

Similarly to previous work by Cusatis (Cusatis et al. 2003; 2011b), the inelastic constitutive laws for each eigenmode are expressed introducing an effective eigenstrain defined as:  $\epsilon^{(I)} = \sqrt{(\epsilon_N^{(I)})^2 + (\epsilon_T^{(I)})^2}$  where  $\epsilon_T^{(I)} = \sqrt{(\epsilon_M^{(I)})^2 + (\epsilon_L^{(I)})^2}$  = total shear strain component of  $I$ th microplane eigenstrain. The relation between the stress and strain microplane components can be found introducing an effective eigenstress,  $\sigma^{(I)}$  and imposing the consistency of the virtual work:

$$\delta \mathcal{W}_I = \sigma^{(I)} \delta \epsilon^{(I)} = \frac{\sigma^{(I)}}{\epsilon^{(I)}} (\epsilon_N \delta \epsilon_N + \epsilon_M \delta \epsilon_M + \epsilon_L \delta \epsilon_L)^{(I)} = (\sigma_N \delta \epsilon_N)^{(I)} + (\sigma_M \delta \epsilon_M)^{(I)} + (\sigma_L \delta \epsilon_L)^{(I)} \quad (16)$$

By means of Eq. (16), the relationship between normal and shear stresses versus normal and shear strains can be formulated through damage-type constitutive equations:

$$\sigma_N^{(I)} = \left( \sigma \frac{\epsilon_N}{\epsilon} \right)^{(I)}, \quad \sigma_M^{(I)} = \left( \sigma \frac{\epsilon_M}{\epsilon} \right)^{(I)}, \quad \sigma_L^{(I)} = \left( \sigma \frac{\epsilon_L}{\epsilon} \right)^{(I)} \quad (17)$$

The effective stress  $\sigma^{(I)}$  is assumed to be incrementally elastic, i.e.  $\dot{\sigma}^{(I)} = \lambda^{(I)} \dot{\epsilon}^{(I)}$  and it is formulated such that  $0 \leq \sigma^{(I)} \leq \sigma_{bi}^{(I)}(\epsilon^{(1)}, \epsilon^{(2)}, \dots, \theta, \varphi)$  where  $\sigma_{bi}^{(I)}(\epsilon^{(1)}, \epsilon^{(2)}, \dots, \theta, \varphi)$  with subscript  $i=t$  for tension and  $i=c$  for compression is a limiting boundary enforced through a vertical (at constant strain) return algorithm. It is worth mentioning here that, in general,  $\sigma_{bi}^{(I)}$  might be a function of the microplane orientation and of the equivalent strains pertaining to other modes. This allows to inherently embed in the formulation the effects of damage anisotropy and the interaction between damaging mechanisms.

#### Inelastic behavior in the fiber direction

Cusatis et al. (2008) showed that the stiffness tensor for a UD composite, treated as transversely isotropic, can be decomposed into 4 energetically orthogonal eigenmodes, each being associated to a particular type of deformation. Mode 1 is related to the normal and shear deformation in out-of-plane direction, mode 2 is related to a macroscopic normal deformation in the direction of the fibers, mode 3 is associated to an in-plane normal deformation orthogonal to the fibers and mode 4 is related to in-plane shear deformation. In this work, it is assumed that failure of FRP happens mainly by fiber fracture and pullout. Accordingly, a strain dependent nonlinear constitutive law is defined for mode 2 whereas elastic behavior is assumed for all the other modes. This assumption is largely supported by the experimental analysis of fracture surfaces of the failed composite jackets. The strain dependent

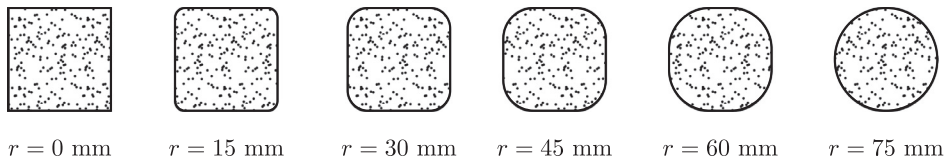


**Fig. 6.** Corner radius variations of the column cross section.

**Table 1**  
Macroscopic material properties.

Property	Concrete	FRP sheet	
		Fiber dir.	Transverse dir.
Modulus of elasticity (MPa)	30,000	230,000	30,000
Poisson's ratio	0.2	-	0.25
Shear modulus (MPa)	-	4,000 <sup>a</sup>	1,300 <sup>a</sup>
Compressive strength (MPa)	31	-	-
Tensile strength (MPa)	3 <sup>a</sup>	3482	-
Fracture energy (N/mm)	0.14 <sup>a</sup>	220 <sup>a</sup>	-

<sup>a</sup> Estimated value.

boundary in tension,  $\varepsilon_N^{(2)} \geq 0$ , can be expressed by the following equations:

$$\sigma_{bt}^{(2)} = s^{(2)}(\theta, \varphi) \exp \left[ - \left( \frac{(\varepsilon_{\max}^{(2-t)} - \varepsilon_{0t}^{(2)})}{k_{bt}^{(2)}} \right)^{a_{t2}} \right] \quad (18)$$

where  $s^{(2)}(\theta, \varphi) = s_0^{(2)} \cos^2(\theta)$  with  $s_0^{(2)}$  = mode 2 microplane tensile strength. The boundary  $\sigma_{bt}^{(2)}$  evolves exponentially as a function of the maximum effective strain, which is a history-dependent variable defined as  $\varepsilon_{\max}^{(2-t)}(t) = \max_{\tau \leq t} [\varepsilon^{(2)}(\tau)]$ . The exponential decay of the boundary  $\sigma_{bt}^{(2)}$  starts when the maximum effective strain reaches its elastic limit  $\varepsilon_{0t}^{(2)}(\theta, \varphi) = s^{(2)}/\lambda^{(2)}$ . For the sake of simplicity, the behavior of FRP is assumed linear elastic in compression, since failure always occurs in tension for the cases under study. The total number of required parameters to describe mode 2 in tension is 3,  $s_0^{(2)}$ ,  $k_{bt}^{(2)}$ ,  $a_{t2}$  and they need to be calibrated according to experimental data.

### 3. Numerical analysis of FRP confined concrete

#### 3.1. Material properties and experimental tests

The experimental tests performed by Wang and Wu (2008) are taken as a reference for the present numerical study, where concrete specimens (width/ height = 150 mm/300 mm) with different corner radii (Fig. 6), unconfined and wrapped by 1 or 2 carbon FRP plies (equivalent thickness per layer  $s = 0.165$  mm), are subjected to compression. The concrete used in the experiments was based on the following mix design:  $c = 280$  kg/m<sup>3</sup> (cement content, estimated),  $w/c = 0.77$  (water to cement ratio),  $a/c = 7.5$  (aggregate to cement ratio, estimated),  $d_a = 10$  mm (max aggregate size),  $n_f = 0.5$  (Fuller curve exponent, estimated). Macroscopic elastic and strength properties of the materials are summarized in Table 1.

After sanding and cleaning the specimen surface, the FRP was wrapped around it by typical manual lay-up procedure, orienting the fibers in the hoop direction and forming one or two layers. Strain gauges were mounted prior to the testing at multiple points at the mid-height of the specimens to measure the strains at different locations of the FRP laminate. Three identical specimens for each condition were tested and the average responses were reported in the publication (Wang and Wu 2008).

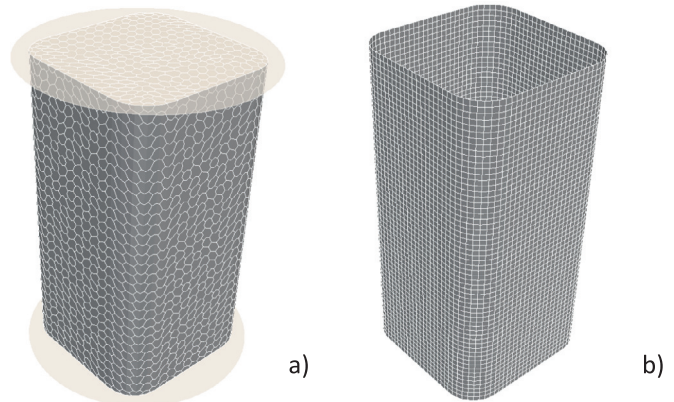


**Fig. 7.** Geometry example of column ( $r = 30$  mm). (a) Concrete column with loading plates, (b) FRP jacket.

#### 3.2. Model generation

As described in Section 2.1, the randomly generated concrete meso-structure is constructed by defining the coarse aggregate particles on the basis of the concrete mix design and the minimum aggregate size ( $d_0 = 5$  mm hereinafter), governing the resolution of the model.

The LDPM parameters, required for the definition of the facet constitutive law (Cusatis et al. 2011b; 2011a), are calibrated through the best fitting of the complete load-displacement curves relevant to different experimental tests. As previously mentioned, in general hydrostatic compression, unconfined compression, fracture test, triaxial compression at low-confinement, triaxial compression at high-confinement are needed for a complete calibration. In the present study, all needed experimental curves were not available from Wang and Wu (2008), consequently some of the parameters were estimated from other available experimental data relevant to the concrete mixes similar to the ones under investigation. The experimental axial stress vs. axial strain curve for circular specimens unconfined and confined with one FRP layer were fitted using the following LDPM parameters:  $E_0 = 40,000$  MPa,  $\alpha = 0.25$ ,  $\sigma_t = 3.65$  MPa,  $l_t = 200$  mm,  $\sigma_s/\sigma_t = 2.5$ ,  $n_t = 0.2$ ,  $\sigma_{c0} = 45$  MPa,  $H_{c0}/E_0 = 0.3$ ,  $\kappa_{c0} = 4$ ,  $\kappa_{c1} = 1$ ,  $\kappa_{c2} = 5$ ,  $H_{c1}/E_0 = 0.1$ ,  $\mu_0 = 0.2$ ,  $\mu_\infty = 0$ ,  $\sigma_{N0} = 600$  MPa,  $E_d/E_0 = 1$ .

In the simulations, the load was applied through steel platens, modeled as rigid bodies, directly in contact with the specimens ends and equipped with a constraint algorithm to simulate high friction conditions. Specifically, the adopted constraint restricts the set of top and bottom nodes of the specimen to move on the top and bottom platen surface, respectively, with a master-slave formulation for the direction perpendicular to the surface and with a stick-slip friction model for the resistance to sliding along the plane. The friction coefficient  $\mu$  is computed as a function of the contact slippage  $v$ ,  $\mu(v) = \mu_d + (\mu_s - \mu_d)v_0/(v_0 + v)$  with the friction parameters optimized for high friction ( $\mu_s = 0.13$ ,  $\mu_d = 0.015$ ,  $v_0 = 1.3$  mm) according to Cusatis et al. 2011a. Fig. 7 shows an example of LDPM discretization and the rigid plates for the boundary conditions.

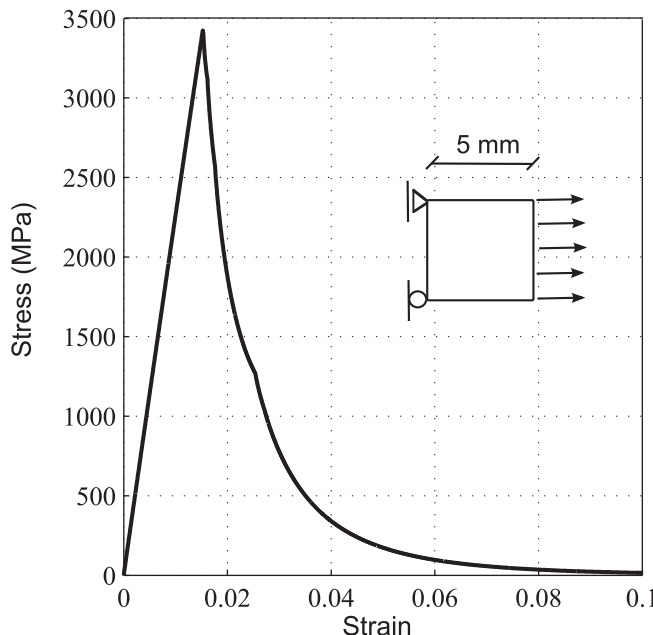


**Fig. 8.** Stress-strain curve in the FRP (fibers direction).

The FRP jackets are modeled by means of quadrilateral shell elements with one in-plane integration point and physical hourglass stabilization (Belytschko and Leviathan 1994) and they are given the orthotropic behavior through the described spectral stiffness microplane model, which allows orienting the fibers in the hoop direction. The mechanical properties of the FRP laminates are assigned according to the manufacturer data (Wang and Wu 2008; Gambarelli et al. 2014) or estimated from literature (Mottram 2004; Gerstle 1991) and the corresponding parameters are reported in Table 1. The parameters of the spectral stiffness microplane model governing the inelastic behavior of the fibers were calibrated according to given ultimate stress and estimated value of fracture energy, according to Salviato et al. (2016) (see Table 1). Spurious mesh sensitivity due to strain localization was avoided by means of the crack band model (Bažant and Oh 1985). For a 5 mm  $\times$  5 mm shell element the calibrated parameters are:  $s_0^{(2)} = 3,482$  MPa,  $k_{bt}^{(2)} = 0.04$ ,  $a_t2 = 0.75$ . The resulting response of the composite in the fiber direction is shown in Fig. 8. Considerations on the interface behavior between concrete column and FRP plies are given in Section 5.1.

#### 4. Considerations on the FRP ultimate condition

Failure of FRP-confined column is always due to the rupture of the FRP jacket, governed by the fracturing tensile strain or tensile strength in the hoop direction (Teng and Lam 2004). The material allows limited stress redistribution because of its elastic brittle character so the identification of the fracturing tensile strain is paramount to understand the column collapse mechanisms. In many existing theoretical or numerical models (Teng et al. 2001; Lam and Teng 2004a) the tensile rupture of FRP is characterized by the hoop strain reaching its fracturing limit as measured from coupon tests. However, different experimental results have shown that the hoop rupture strains of FRP measured in FRP-confined columns are on average significantly lower than coupon failure strains (see Smith et al. 2010; Xiao and Wu 2000; Pessiki et al. 2001; Shahawy et al. 2000). In particular, Wang and Wu (2008) report a FRP fracturing strain at least 25% lower than the one measured on coupons and that the reduction is more significant (a) in the corners and (b) in case of multiple layers. A systematic

analysis of the factors influencing the fracturing condition of FRP-wrapped concrete columns is given by Chen et al. (2013), where different causes were highlighted to affect the composite rupture. They are herein briefly listed: (1) geometrical factors, such as geometrical discontinuities, FRP overlap region, geometrical imperfections and curvature of the FRP jacket; (2) FRP material factors, such as unintentional fiber misorientation, misalignment and uneven tension of fibers, damage of fibers, triaxial stress state in the FRP; (3) concrete material factors, such as nonuniform deformation and strain localization in concrete; (4) adhesive material and geometry factors, such as mechanical properties and geometrical details of the adhesive; (5) loading factors, such as eccentric or non uniform loading, stressing attributable to thermal deformation and creep.

The numerical model developed in the present paper is able to account for the concrete material factors, being LDPM a meso-scale model. LDPM captures naturally the non uniform local deformations on concrete, leading to non uniform strain deformation in the FRP, in both the circumferential and axial direction. Consequently, FRP strain localization resulting from concrete cracking can be also simulated. However, the FRP jacket is modeled with orthotropic shell elements of equivalent thickness  $s = 0.165$  mm/layer and the tensile properties of a wet layup processed FRP are assigned on the basis of the nominal thickness of the fiber/fabric sheet, because the actual thickness is difficult to control and the resin contribution is relatively small (Lam and Teng 2004b). For these reasons, the numerical simulations in this study cannot include any FRP material or geometrical factors related to fibers or matrix.

#### 5. Results and discussion

##### 5.1. Preliminary study on the FRP-concrete interface

In a preliminary study, different types of formulations for the FRP-concrete interaction were examined, by using the square and the circular shaped columns wrapped by 1 layer of composite. In particular, the following options were explored in order to evaluate the sensitivity of the model to the interface behavior. The first option (1) consists of a master-slave formulation where the FRP nodes (slaves) are forced to lay on the external lateral surface of the concrete column (master) and both normal and tangential forces are transferred. This means that not slippage is allowed at the interface, corresponding to cases in which debonding does not occur. In the second option (2), a master-slave formulation is still used but the nodes of the external lateral surface of the concrete column (slaves) are forced to lay on the internal lateral surface of the FRP jacket (master) and both normal and tangential forces are transferred. Again, no slippage at the interface is allowed. The third option (3) is characterized by master-slave formulation where the FRP nodes (slaves) are forced to lay on the external lateral surface of the concrete column (master) and only normal forces are transferred. This means that relative slippage at the interface can occur freely, representing a fully debonded situation. The final option (4) is similar to (3) but the nodes of the external lateral surface of the concrete column (slaves) are forced to lay on the internal lateral surface of the FRP jacket (master).

Rotations of FRP shell elements and LDPM particles are not constrained in any of the 4 cases.

The comparison in terms of axial stress vs. axial strain curves is shown in Fig. 9. Results in Fig. 9a shows that it is more appropriate to consider the lateral surface of concrete column as master and the FRP as slave, in the contact definition. As a matter of fact, curves (2) and (4) do not describe properly the behavior of the circular column because the confining effect provided by the jacket is considerably underestimated. The response is much more realistic in case of curves (1) and (3), as it emerges from the comparison

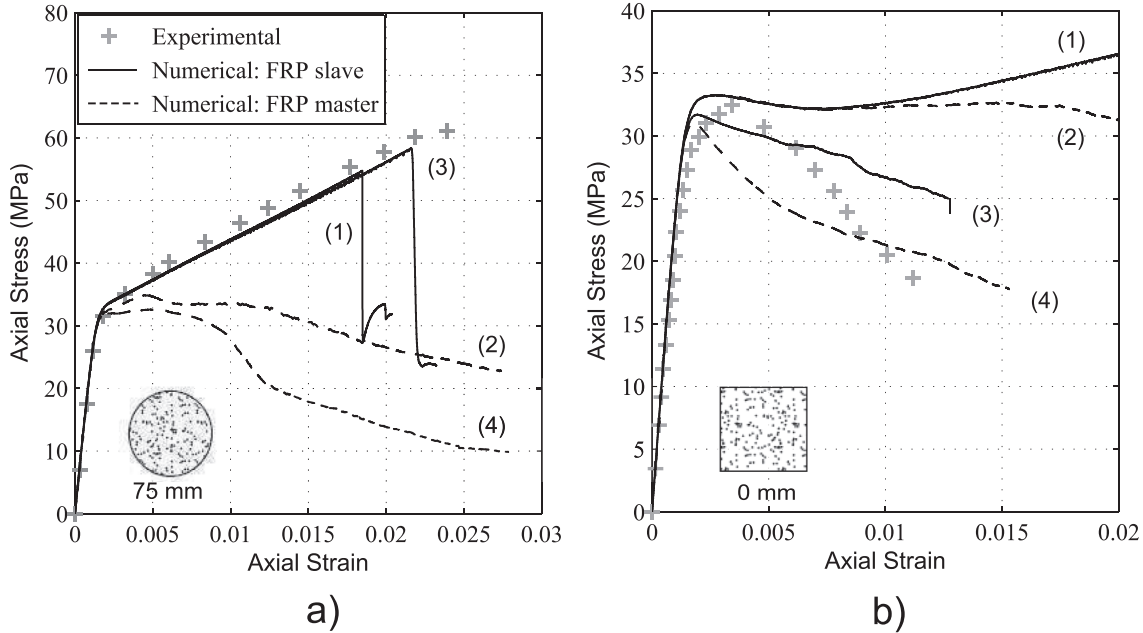


**Fig. 9.** Comparison between experimental and numerical stress vs. strain curves for (a) the square column ( $r = 0 \text{ mm}$ ) and (b) the circular column ( $r = 75 \text{ mm}$ ) with 1 FRP ply. (1), (2), (3), (4) correspond to various type of FRP-concrete contact algorithm, as described in the text.

with the experimental data, and it does not change significantly whether the tangential component is taken into account or not. This results indicate that the circular columns are less sensitive to debonding due to the symmetric character of the deformation process, at least prior to failure. In Fig. 9b, the comparison between curve (1) and (3) shows that, for square columns, the confinement effect decreases substantially when the tangential interaction between the surfaces is neglected. This proves that the debonding mechanisms play a major role due to the discontinuities associated with sharp corners.

According to these observations, one can conclude that the development of a proper contact algorithm for the bond, able to capture the progressive debonding effects, is indeed important, especially for the right-cornered sections. In the examples discussed in the following sections, the interaction between the concrete columns and the FRP plies is modeled with the type (1) algorithm in case of larger corner radius. For the columns with smaller corner radius, the predictions with algorithm (1) and (3), are compared and discussed.

## 5.2. Response of columns with larger corner radius

The uniaxial stress-strain curves in Fig. 10 are relevant to specimens with corner radius from  $r = 30 \text{ mm}$  to  $r = 75 \text{ mm}$ . Experimental and the numerical responses of unconfined and FRP-confined concrete columns (with 1 layer and 2 layers) are compared for each cross section. Similarly to the experiments, the axial stress is obtained by dividing the global axial displacement over the specimen height and the lateral strain as an average of the radial displacements over the undeformed radial length, measured at the middle of each side face and at half-height of the specimen. The results show that, after the calibration of the parameters through the unconfined concrete loading curves and the response of the circular columns, the model can capture the behavior of concrete columns in compression subjected to uniform and non-uniform confinement at different levels. As well-known from the majority of existing experimental tests, the axial stress-axial strain curves of FRP-confined concrete are characterized by a monoton-

ically hardening bilinear shape, where the change in shape occurs always at a stress level close to the unconfined concrete compressive strength, as opposed to feature a softening branch typical of actively confined concrete at low confinement. As the axial stress increases, the confining pressure provided by the jacket also increases instead of remaining constant and if the stiffness of FRP exceeds a certain threshold value, this confining pressure increases fast enough to ensure that the stress-strain curve is monotonically hardening. Naturally, the higher is the FRP stiffness, the higher is the slope of the second branch, as shown by the typical evolution of stress vs. strain captured for different number of FRP layers. This feature of the response is well captured by the current model. The corner radius effect is also captured and higher post peak stiffness is observed for columns with a larger corner radius, in both experiments and simulations. Fig. 11 shows stress and strain distributions in the FRP jacket at the ultimate condition for the different columns. All the columns fail by tensile rupture of the FRP wrap in the midheight region and rupture originates from the vicinity of the corners, as seen in the experiments (e.g. Wang et al. 2012; Dalgic et al. 2016; Wang and Wu 2008). In Fig. 12, the fracture patterns developed in the concrete columns are reported through the plotting of the meso-scale crack opening. Before the FRP rupture, the damage in concrete is symmetrically distributed according to the geometry and it gradually increases with the reduction of the corner radius, especially along the sides of the specimens according to the reduction of the confinement effects. With the FRP rupture, the symmetry of the response is completely lost: strain and damage localization occur with the sudden growing of an inclined fracture in the FRP jacket and consequently a shear band in the concrete element, causing the collapse of the specimen. The ultimate stress and strain values, together with the failure modes, are captured with very good approximation by the proposed model (see Fig. 10), proving that the combination of LDPM and SMPM can provide a numerical tool more powerful and realistic than the majority of the existing FE models for FRP-confined concrete.

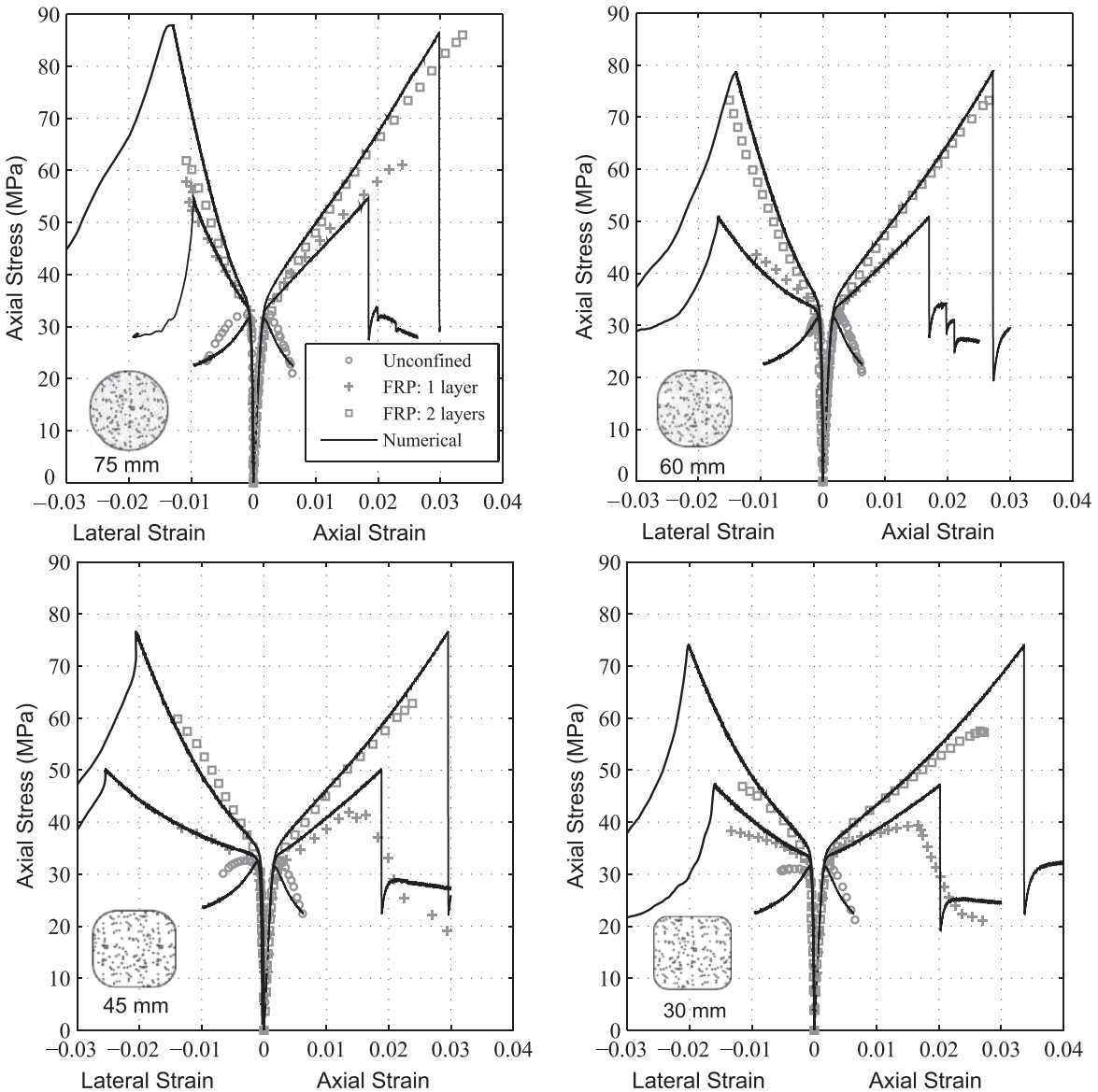


**Fig. 10.** Stress vs. strain curves for columns with larger corner radius.

### 5.3. Response of columns with smaller corner radius

The overall behavior of the columns with the smallest corner radius ( $r = 15 \text{ mm}$  and  $r = 0 \text{ mm}$ ) is shown in Fig. 13. The experimental stress-strain curves lack the characteristic bilinear trend, typical of FRP-confined rounded columns; instead, they have a softening tendency after the peak due to the progressive rupture and debonding of the jacketing, which is able to provide some increased ductility but not additional strength.

The numerical curves obtained without allowing debonding (contact type 1) generally overestimate both the confining effect and the stress level at which failure of the FRP occurs. On the contrary, these two features are both underestimated when tangential debonding is assumed from the beginning of the simulation (contact type 3). Therefore, confirming what was preliminary observed, a more sophisticated formulation of the FRP-concrete bond is required for sharp cornered columns, to be able to predict the progressive debonding mechanisms occurring at the interface. Such failure mechanisms, very uncommon for more round shaped columns, significantly decreases the effectiveness of the strengthening (Buyukozturk et al. 2004), especially if the debonding inter-

acts with the local rupture of the composite. Furthermore, it has been recently pointed out by Gambarelli et al. (2014) that not only delamination between matrix and concrete surface, but also between matrix and carbon fibers might occur, especially close to the corners, making the modeling of the interface even more complex.

Nonetheless, the current model can capture an interesting aspect of the behavior if debonding is prevented. The confining effect in square columns is highly non uniform and not very effective, therefore, a descending branch in the stress-strain curve is possible at stress levels close to the compressive strength, even if the FRP does not debond or fracture. This happens "because the dilation of concrete on the straight sides may only cause a slight bulging of the FRP jacket without significantly mobilizing its membrane action" (Wu and Zhou 2010). Further increase in stress usually occurs later, with the increase of lateral deformation and, consequently, of the confinement pressure to a level sufficient to generate the hardening response. This phenomenon has been observed and described in literature (Jiang and Teng 2007) and it is well captured by the simulation (Fig. 13). In addition, as previously mentioned in Section 4, the proposed approach cannot take into account the FRP material or geometrical factors related to the fibers

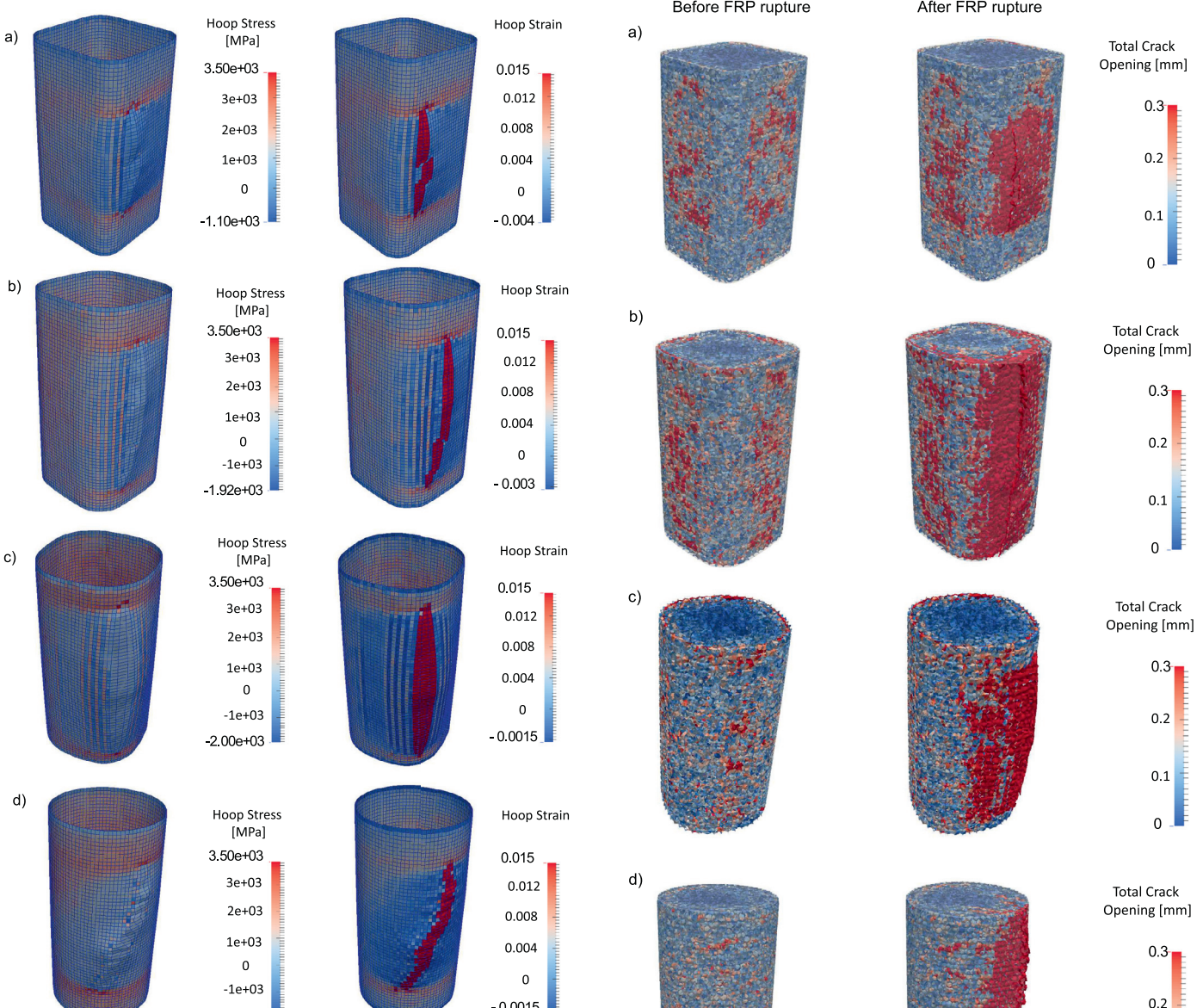


**Fig. 11.** Hoop stress and strain distribution in the FRP at the ultimate condition for (a)  $r = 30 \text{ mm}$ , (b)  $r = 45 \text{ mm}$ , (c)  $r = 60 \text{ mm}$ , (d)  $r = 75 \text{ mm}$ .

or adhesive that lead to the rupture of the composite and, consequently, to the column collapse. These factors tend to have a more important effect in the case of sharp corner columns. The jacket is modeled with orthotropic shell elements of nominal thickness  $s = 0.165 \text{ mm}/\text{layer}$ , being the actual thickness difficult to control and the contribution of the matrix relatively small (Lam and Teng 2004b). However, neglecting the matrix contribution when a substantial difference between the nominal and the actual thickness occurs can lead to inaccurate approximations in the composite response. For instance, the flexural behavior, and the consequent triaxial stress state, cannot be modeled accurately in the case of sharp-angled cross sections, where the FRP soon experiences high local stress concentrations and local damage accumulation.

## 6. Conclusions and further research

A three-dimensional framework for the numerical simulation of concrete columns confined by FRP loaded in compression has been presented in this paper. The approach is based on a meso-scale

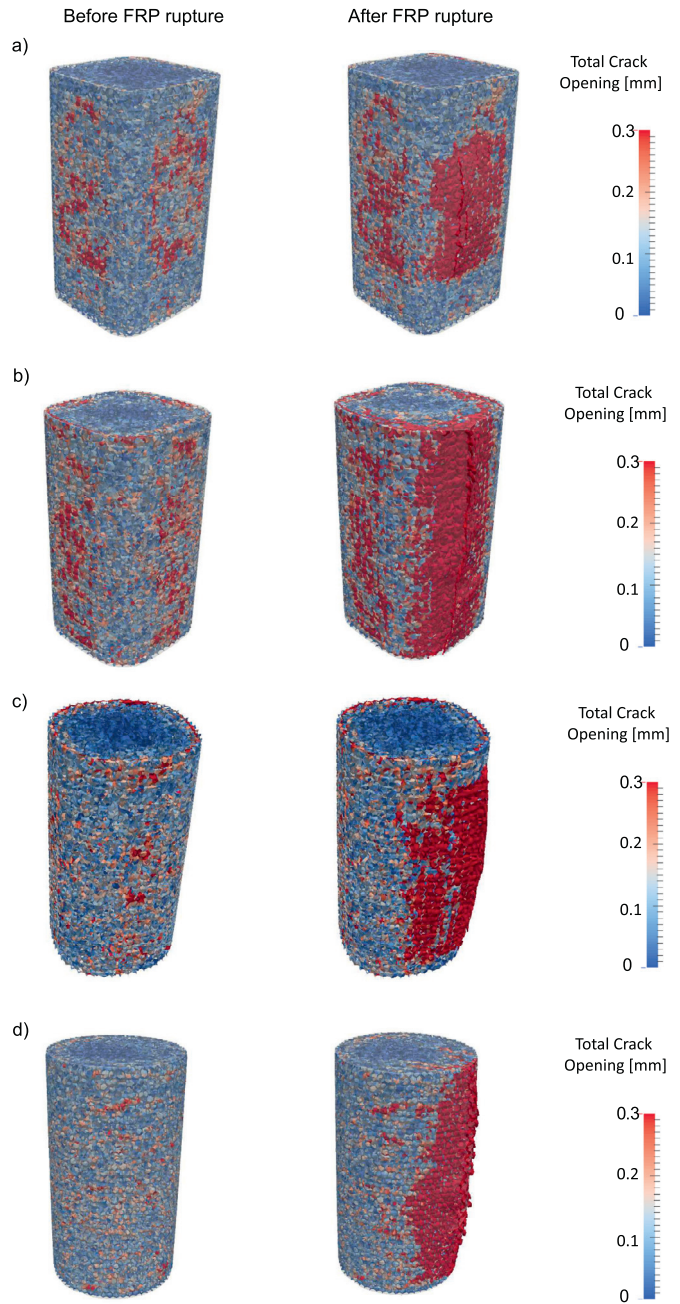


**Fig. 12.** Crack Opening in the concrete columns for (a)  $r = 30 \text{ mm}$ , (b)  $r = 45 \text{ mm}$ , (c)  $r = 60 \text{ mm}$ , (d)  $r = 75 \text{ mm}$ .

model for concrete, the Lattice Discrete Particle Model (LDPM) and a microstructural inspired constitutive equation for FRP, the Spectral Microplane Model (SMPM). With the described improvement of the constitutive law in compression for LDPM and after the parameters calibration, the model can predict the behavior of FRP confined concrete and its sensitivity to the stiffness of the FRP wrapping and to the shape of the cross section. With reference to the experimental data used for this study, the response of the specimens with largest corner radius (from  $r = 30 \text{ mm}$  to  $r = 75 \text{ mm}$ ) is accurately described, not only in terms of stress vs. strain curves but also in terms of ultimate condition, which is captured with a very good accuracy for the different cross sections. The model can realistically capture the fracture patterns developing in concrete during the loading history and the failure modes related to the FRP jacket fracture. The specimens with sharpest corner ra-

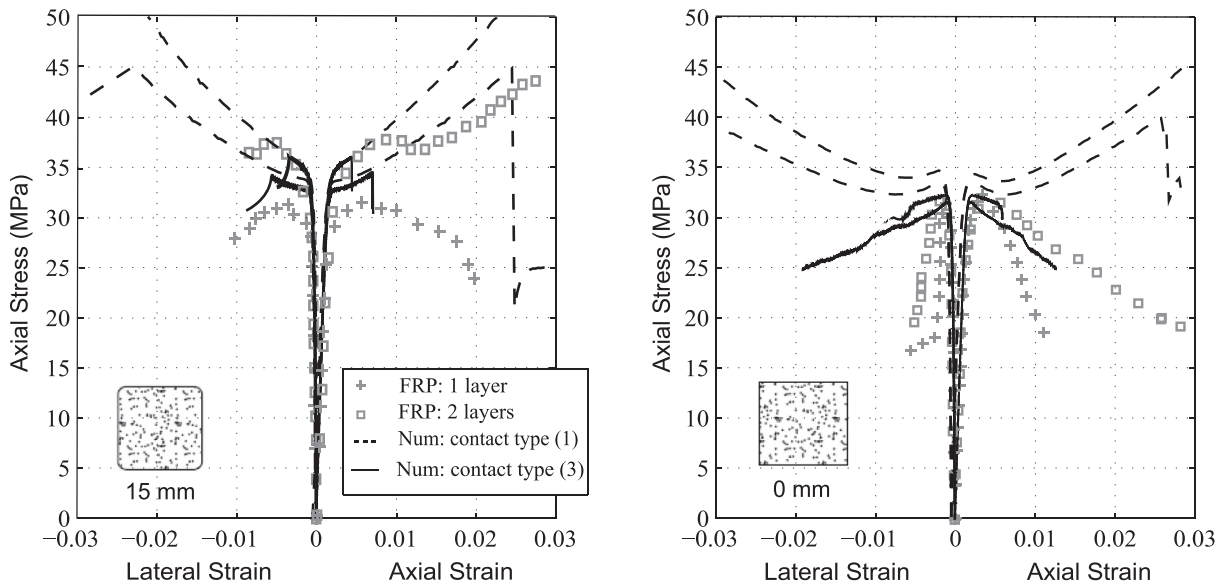


**Fig. 13.** Stress vs. strain curves for columns with smaller corner radius.

dius ( $r = 0 \text{ mm}$  and  $r = 15 \text{ mm}$ ), instead, require a more advanced modeling of the FRP jacket and, in particular, of the contact between FRP and concrete in order to capture the complex phenomena related to the local stress concentrations and FRP debonding processes. In fact, it has been observed that not allowing debonding between FRP and concrete generally lead to an overestimation of the confining effect and the stress level at FRP failure, while these two features are both underestimated if tangential debonding is assumed since the beginning of the simulation. This difference is neither observed in the experiment nor predicted by the model for large radius columns.

Contrarily to most models in the literature that tackle only specific aspects of FRP reinforcing, the model presented in this effort has potential to provide a complete and general computational framework. The key factors for a successful simulation of FRP-concrete systems are related to the modeling of (a) concrete material, (b) FRP material, (c) FRP-concrete interface. The results in this paper show that the formulated model successfully addresses the first two aspects, while the last requires further improvements that will be pursued in the near future.

## Acknowledgments

The work of the last author was partially supported by the National Science Foundation under grant no. CMMI-1435923. The authors would like to thank ES3, Engineering and Software System Solutions, Inc. for the computational support with the software MARS and Prof. J. G. Teng and Prof. C. Carloni for stimulating discussions.

## References

- Alnagar, M., Cusatis, G., Di Luzio, G., 2013. Lattice discrete particle modeling (LDPM) of alkali silica reaction (ASR) deterioration of concrete structures. *Cem. Concr. Compos.* 41, 45–59. <http://dx.doi.org/10.1016/j.cemconcomp.2013.04.015>
- Bažant, Z.P., Caner, F.C., Carol, I., Adley, M.D., Akers, S.A., 2000. Microplane model M4 for concrete. i: formulation with work-conjugate deviatoric stress. *J. Eng. Mech.* 126 (9), 944–953. doi:[10.1061/\(ASCE\)0733-9399\(2000\)126:9\(944\)](https://doi.org/10.1061/(ASCE)0733-9399(2000)126:9(944)).
- Bažant, Z.P., Di Luzio, G., 2004. Nonlocal microplane model with strain-softening yield limits. *Int. J. Solids Struct.* 41 (24–25), 7209–7240. doi:[10.1016/j.ijsolstr.2004.05.065](https://doi.org/10.1016/j.ijsolstr.2004.05.065).
- Bažant, Z.P., Oh, B.H., 1985. Microplane model for progressive fracture of concrete and rock. *J. Eng. Mech.* 111 (4), 559–582. [http://dx.doi.org/10.1061/\(ASCE\)0733-9399\(1985\)111:4\(559\)](http://dx.doi.org/10.1061/(ASCE)0733-9399(1985)111:4(559)).
- Bažant, Z.P., Prat, P.C., 1988. Microplane model for brittle plastic material: i theory. *J. Eng. Mech.* 114 (10), 1672–1688. [http://dx.doi.org/10.1061/\(ASCE\)0733-9399\(1988\)114:10\(1672\)](http://dx.doi.org/10.1061/(ASCE)0733-9399(1988)114:10(1672)).
- Belytschko, T., Leviathan, I., 1994. Physical stabilization of the 4-node shell element with one point quadrature. *Comput. Methods Appl. Mech. Eng.* 113 (3–4), 321–350. [http://dx.doi.org/10.1016/0045-7825\(94\)90052-3](http://dx.doi.org/10.1016/0045-7825(94)90052-3).
- Binici, B., 2005. An analytical model for stress-strain behavior of confined concrete. *Eng. Struct.* 27 (7), 1040–1051. <http://dx.doi.org/10.1016/j.engstruct.2005.03.002>.
- Buyukozturk, O., Gunes, O., Karaca, E., 2004. Progress on understanding debonding problems in reinforced concrete and steel members strengthened using FRP composites. *Constr. Build. Mater.* 18 (9–19). doi:[10.1016/S0950-0618\(03\)00094-1](https://doi.org/10.1016/S0950-0618(03)00094-1).
- Caner, F.C., Bažant, Z.P., 2012. Microplane model M7 for plain concrete. i: formulation. *J. Eng. Mech.* 139 (12), 1714–1723. [http://dx.doi.org/10.1061/\(ASCE\)EM.1943-7889.0000570](http://dx.doi.org/10.1061/(ASCE)EM.1943-7889.0000570).
- Carol, I., Bažant, Z.P., 1997. Damage and plasticity in microplane theory. *Int. J. Solids Struct.* 34 (29), 3807–3835. [http://dx.doi.org/10.1016/S0020-7683\(96\)00238-7](http://dx.doi.org/10.1016/S0020-7683(96)00238-7).
- Chen, J., Li, S., Bisby, L., 2013. Factors affecting the ultimate condition of FRP-wrapped concrete columns. *J. Compos. Constr.* 17 (1), 67–78. doi:[10.1061/\(ASCE\)CC.1943-5614.0000314](https://doi.org/10.1061/(ASCE)CC.1943-5614.0000314).
- Cusatis, G., Bažant, Z., Cedolin, L., 2003. Confinement-shear lattice model for concrete damage in tension and compression: i. theory. *J. Eng. Mech.* 129 (12), 881–889.
- Cusatis, G., Beghini, A., Bažant, Z., 2008. Spectral stiffness microplane model for quasibrittle composite laminates-part i: theory. *J. Appl. Mech.* 75 (2), 021009. <http://dx.doi.org/10.1115/1.2744036>.
- Cusatis, G., Mencarelli, A., Pelessone, D., Baylott, J.T., 2011a. Lattice discrete particle model (LDPM) for failure behavior of concrete. II: calibration and validation. *Cem. Concr. Compos.* 33 (9), 891–905. <http://dx.doi.org/10.1016/j.cemconcomp.2011.02.010>.
- Cusatis, G., Pelessone, D., Mencarelli, A., 2011b. Lattice discrete particle model (LDPM) for failure behavior of concrete. i: theory. *Cem. Concr. Compos.* 33 (9), 881–890. <http://dx.doi.org/10.1016/j.cemconcomp.2011.02.011>.
- Cusatis, G., Zhou, X., 2014. High-order microplane theory for quasi-brittle materials with multiple characteristic lengths. *J. Eng. Mech.* 140 (7), 04014046. doi:[10.1061/\(ASCE\)EM.1943-7889.0000747](https://doi.org/10.1061/(ASCE)EM.1943-7889.0000747).
- Dalgic, K., Ispir, M., Ilki, A., 2016. Cyclic and monotonic compression behavior of CFRP-jacketed damaged noncircular concrete prisms. *J. Compos. Constr.* 20 (1), 04015040. doi:[10.1061/\(ASCE\)CC.1943-5614.0000603](https://doi.org/10.1061/(ASCE)CC.1943-5614.0000603).
- Desprez, C., Mazars, J., Kotronis, P., Paultre, P., 2013. Damage model for FRP-confined concrete columns under cyclic loading. *Eng. Struct.* 48, 519–531. <http://dx.doi.org/10.1016/j.engstruct.2012.09.019>.
- Di Luzio, G., 2007. A symmetric over-nonlocal microplane model M4 for fracture in concrete. *Int. J. Solids Struct.* 44 (13), 4418–4441. <http://dx.doi.org/10.1016/j.ijsolstr.2006.11.030>.
- Di Luzio, G., Cusatis, G., 2013. Solidification – microprestress – microplane (SMM) theory for concrete at early age: theory, validation and application. *Int. J. Solids Struct.* 50 (6), 957–975. <http://dx.doi.org/10.1016/j.ijsolstr.2012.11.022>.
- Elsanadedy, H.M., Al-Salloum, Y.A., Alsayed, S.H., Iqbal, R.A., 2012. Experimental and numerical investigation of size effects in FRP-wrapped concrete columns. *Constr. Build. Mater.* 29, 56–72. <http://dx.doi.org/10.1016/j.conbuildmat.2011.10.025>.
- Fam, A., Rizkalla, S., 2001. Confinement model for axially loaded concrete confined by circular fiber-reinforced polymer tubes. *ACI Struct. J.* 98 (4), 451–461.

- Gambarelli, S., Nisticò, N., Ožbolt, J., 2014. Numerical analysis of compressed concrete columns confined with CFRP: microplane-based approach. Composites Part B 67, 303–312. <http://dx.doi.org/10.1016/j.compositesb.2014.06.026>.
- Gerstle, F.P., 1991. "Composites", Encyclopedia of polymer science and engineering. J. Wiley & sons, New York.
- Harajli, M.H., 2006. Axial stress-strain relationship for FRP confined circular and rectangular concrete columns. Cem. Concr. Compos. 28 (10), 938–948. <http://dx.doi.org/10.1016/j.cemconcomp.2006.07.005>. Durability and Ductility of FRP Strengthened Beams, Slabs and Columns
- Jiang, J.-F., Wu, Y.-F., 2012. Identification of material parameters for drucker-prager plasticity model for FRP confined circular concrete columns. Int. J. Solids Struct. 49 (3–4), 445–456. <http://dx.doi.org/10.1016/j.ijsolstr.2011.10.002>.
- Jiang, T., Teng, J., 2007. Analysis-oriented stress-strain models for FRP-confined concrete. Eng. Struct. 29 (11), 2968–2986. <http://dx.doi.org/10.1016/j.engstruct.2007.01.010>.
- Karabinis, A., Rousakis, T., 2002. Concrete confined by FRP material: a plasticity approach. Eng. Struct. 24 (7), 923–932. doi:[10.1016/S0141-0296\(02\)00011-1](https://doi.org/10.1016/S0141-0296(02)00011-1).
- Karabinis, A.I., Rousakis, T.C., Manolitsi, G.E., 2008. 3D finite-element analysis of substandard RC columns strengthened by fiber-reinforced polymer sheets. J. Compos. Constr. 12 (5), 531–540.
- Koksal, H., Doran, B., Turgay, T., 2009. A practical approach for modeling FRP wrapped concrete columns. Constr. Build. Mater. 23 (3), 1429–1437. <http://dx.doi.org/10.1016/j.conbuildmat.2008.07.008>.
- Lam, L., Teng, J., 2003. Design-oriented stress-strain model for FRP-confined concrete. Constr. Build. Mater. 17 (6–7), 471–489. [http://dx.doi.org/10.1016/S0950-0618\(03\)00045-X](http://dx.doi.org/10.1016/S0950-0618(03)00045-X). Fibre Reinforced Polymer composites in construction
- Lam, L., Teng, J., 2004a. Ultimate condition of fiber reinforced polymer-confined concrete. J. Compos. Constr. 8 (6), 539–548. doi:[10.1016/ASCE\)1090-0268\(2004\)8:6\(539](https://doi.org/10.1016/ASCE)1090-0268(2004)8:6(539).
- Lam, L., Teng, J., 2004b. Ultimate condition of fiber reinforced polymer-confined concrete. J. Compos. Constr. 8 (6), 539–548. doi:[10.1016/ASCE\)1090-0268\(2004\)8:6\(539](https://doi.org/10.1016/ASCE)1090-0268(2004)8:6(539).
- Malej, M., Tanwongsval, S., Paramasivam, P., 2003. Modelling of rectangular RC columns strengthened with FRP. Cem. Concr. Compos. 25 (2), 263–276. [http://dx.doi.org/10.1016/S0958-9465\(02\)00017-3](http://dx.doi.org/10.1016/S0958-9465(02)00017-3).
- Mirmiran, A., Zagers, K., Yuan, W., 2000. Nonlinear finite element modeling of concrete confined by fiber composites. Finite Elem. Anal. Des. 35 (1), 79–96. doi:[10.1016/S0168-874X\(99\)00056-6](https://doi.org/10.1016/S0168-874X(99)00056-6).
- Moran, D.A., Pantelides, C.P., 2012. Elliptical and circular FRP -confined concrete sections: a mohr-coulomb analytical model. Int. J. Solids Struct. 49 (6), 881–898. <http://dx.doi.org/10.1016/j.ijsolstr.2011.12.012>.
- Mottram, J., 2004. Shear modulus of standard pultruded fiber reinforced plastic material. J. Compos. Constr. 8 (2), 141–147.
- Ozbakkaloglu, T., Lim, J.C., 2013. Axial compressive behavior of FRP-confined concrete: experimental test database and a new design-oriented model. Composites Part B 55, 607–634. <http://dx.doi.org/10.1016/j.compositesb.2013.07.025>.
- Pellessone, D., 2015. MARS, Modeling and analysis of the response of structures. User's manual. ES3 Inc.
- Pellegrino, C., Modena, C., 2010. Analytical model for FRP confinement of concrete columns with and without internal steel reinforcement. J. Compos. Constr. 14 (6), 693–705. [http://dx.doi.org/10.1016/ASCE\)CC.1943-5614.0000127](http://dx.doi.org/10.1016/ASCE)CC.1943-5614.0000127).
- Pessiki, S., Harries, K.A., Kestner, J.T., Sause, R., Ricles, J.M., 2001. Axial behavior of reinforced concrete columns confined with FRP jackets. J. Compos. Constr. 5 (4), 237–245. doi:[10.1016/ASCE\)1090-0268\(2001\)5:4\(237](https://doi.org/10.1016/ASCE)1090-0268(2001)5:4(237).
- Rousakis, T., Karabinis, A., Kioussis, P., 2007. FRP-Confined concrete members: axial compression experiments and plasticity modelling. Eng. Struct. 29 (7), 1343–1353. doi:[10.1016/j.engstruct.2006.08.006](https://doi.org/10.1016/j.engstruct.2006.08.006).
- Rousakis, T.C., Karabinis, A.I., Kioussis, P.D., Tepfers, R., 2008. Analytical modelling of plastic behaviour of uniformly FRP confined concrete members. Composites Part B 39 (7–8), 1104–1113. <http://dx.doi.org/10.1016/j.compositesb.2008.05.001>.
- Rousakis, T.C., Rakitzis, T.D., Karabinis, A.I., 2012. Design-oriented strength model for FRP-confined concrete members. J. Compos. Constr. 16 (6), 615–625. [http://dx.doi.org/10.1016/ASCE\)CC.1943-5614.0000295](http://dx.doi.org/10.1016/ASCE)CC.1943-5614.0000295).
- Rychlewski, J., 1995. Unconventional approach to linear elasticity. Arch. Mech. 47, 149–171.
- Salviato, M., Ashari, S.E., Cusatis, G., 2016. Spectral stiffness microplane model for damage and fracture of textile composites. Compos. Struct. 137, 170–184. <http://dx.doi.org/10.1016/j.compstruct.2015.10.033>.
- Schaaffert, E.A., Cusatis, G., 2011. Lattice discrete particle model for fiber-reinforced concrete. i: theory. J. Eng. Mech. 138 (7), 826–833. [http://dx.doi.org/10.1061/\(ASCE\)EM.1943-7889.0000387](http://dx.doi.org/10.1061/(ASCE)EM.1943-7889.0000387).
- Schaaffert, E.A., Cusatis, G., Pelessone, D., O'Daniel, J.L., Baylot, J.T., 2012. Lattice discrete particle model for fiber-reinforced concrete. II: tensile fracture and multi-axial loading behavior. J. Eng. Mech. 138 (7), 834–841. [http://dx.doi.org/10.1061/\(ASCE\)EM.1943-7889.0000392](http://dx.doi.org/10.1061/(ASCE)EM.1943-7889.0000392).
- Shahawy, M., Mirmiran, A., Beitelman, T., 2000. Tests and modeling of carbon-wrapped concrete columns. Composites Part B 31 (6–7), 471–480. [http://dx.doi.org/10.1016/S1359-8368\(00\)00021-4](http://dx.doi.org/10.1016/S1359-8368(00)00021-4).
- Smith, J., Jin, C., Pelessone, D., Cusatis, G., 2015. Dynamics simulations of concrete and concrete structures through the lattice discrete particle model, pp. 63–74. doi:[10.1061/9780784479117.006](https://doi.org/10.1061/9780784479117.006).
- Smith, S.T., Kim, S.J., Zhang, 2010. Behavior and effectiveness of FRP wrap in the confinement of large concrete cylinders. J. Compos. Constr. 14 (5), 573–582. doi:[10.1061/ASCE\)CC.1943-5614.0000119](https://doi.org/10.1061/ASCE)CC.1943-5614.0000119).
- Teng, J., Huang, Y., Lam, L., Ye, L., 2007. Theoretical model for fiber-reinforced polymer-confined concrete. J. Compos. Constr. 11 (2), 201–210. doi:[10.1061/ASCE\)1090-0268\(2007\)11:2\(201](https://doi.org/10.1061/ASCE)1090-0268(2007)11:2(201).
- Teng, J., Lam, L., 2004. Behavior and modeling of fiber reinforced polymer-confined concrete. J. Struct. Eng. 130 (11), 1713–1723. [http://dx.doi.org/10.1061/\(ASCE\)0733-9445\(2004\)130:11\(1713\)](http://dx.doi.org/10.1061/(ASCE)0733-9445(2004)130:11(1713).
- Teng, J., Lam, L., Lin, G., Lu, J., Xiao, Q., 2015a. Numerical simulation of FRP-jacketed RC columns subjected to cyclic and seismic loading. J. Compos. Constr. 19, 15–28. <http://dx.doi.org/10.1016/j.compositesb.2015.03.030>.
- Teng, J.G., Chen, J.F., Smith, S.T., Lam, L., 2001. FRP: Strengthened RC structures. Addison-Wesley.
- Theocaris, P.S., Sokolis, D.P., 1998. Spectral decomposition of the compliance tensor for anisotropic plates. J. Elast. 51 (2), 89–103.
- Theocaris, P.S., Sokolis, D.P., 1999. Spectral decomposition of the linear elastic tensor for monoclinic symmetry. Acta Crystallogr. Sect. A 55 (4), 635–647. doi:[10.1107/S0108767398016766](https://doi.org/10.1107/S0108767398016766).
- Theocaris, P.S., Sokolis, D.P., 2000. Spectral decomposition of the compliance fourth-rank tensor for orthotropic materials. Arch. Appl. Mech. 70 (4), 289–306. <http://dx.doi.org/10.1007/s004199900066>.
- Wang, L.-M., Wu, Y.-F., 2008. Effect of corner radius on the performance of CFRP-confined square concrete columns: test. Eng. Struct. 30 (2), 493–505. <http://dx.doi.org/10.1016/j.engstruct.2007.04.016>.
- Wang, Z., Wang, D., Smith, S.T., Lu, D., 2012. CFRP-Confined square RC columns. i: experimental investigation. J. Compos. Constr. 16 (2), 150–160. doi:[10.1061/ASCE\)CC.1943-5614.0000245](https://doi.org/10.1061/ASCE)CC.1943-5614.0000245).
- Wu, Y., Zhou, Y., 2010. Unified strength model based on Hoek-Brown failure criterion for circular and square concrete columns confined by FRP. J. Compos. Constr. 14 (2), 175–184. doi:[10.1061/ASCE\)CC.1943-5614.0000062](https://doi.org/10.1061/ASCE)CC.1943-5614.0000062).
- Wu, Y.-F., 2015. Development of constitutive models for FRP confined concrete structures, 1, p. 90.
- Xiao, Y., Wu, H., 2000. Compressive behavior of concrete confined by carbon fiber composite jackets. J. Mater. Civ. Eng. 12 (2), 139–146. doi:[10.1061/ASCE\)0899-1561\(2000\)12:2\(139\)](https://doi.org/10.1061/ASCE)0899-1561(2000)12:2(139).
- Yu, T., Teng, J., Wong, Y., Dong, S., 2010a. Finite element modeling of confined concrete i: drucker-prager type plasticity model. Eng. Struct. 32 (3), 665–679. doi:[10.1016/j.engstruct.2009.11.014](https://doi.org/10.1016/j.engstruct.2009.11.014).
- Yu, T., Teng, J., Wong, Y., Dong, S., 2010b. Finite element modeling of confined concrete II: plastic-damage model. Eng. Struct. 32 (3), 680–691. doi:[10.1016/j.engstruct.2009.11.013](https://doi.org/10.1016/j.engstruct.2009.11.013).



**Chiara Ceccato** received her undergraduate and graduate (Master) degrees in civil engineering at University of Padova, Italy, where she is now a PhD candidate. She was a visiting scholar at Northwestern University (Evanston, IL, USA), studying meso-scale models for quasi-brittle materials. Her research interests mainly lie in computational mechanics applied to concrete and FRP materials.



**Marco Salvato** received his PhD degree in Mechanical Engineering from University of Padova (Italy) in 2013. His doctoral research focused on the formulation of multi-scale computational models and the experimental characterization of the mechanical behavior of polymer nanocomposites. Before joining University of Washington in 2015 as assistant professor, Dr. Salvato worked at the Department of Civil and Environmental Engineering at Northwestern University first as a Postdoctoral Fellow, and later as Research Assistant Professor. Currently, he leads the Laboratory for Multiscale Analysis of Materials and Structures at the William E. Boeing Department of Aeronautics and Astronautics. His research focuses on the development of materials with unprecedented mechanical and functional properties and the formulation of computational models to assist the design of the next-generation aerospace structures.



**Carlo Pellegrino** is Full Professor of Structural Analysis and Design and Head of the Department of Civil, Environmental and Architectural Engineering, University of Padova, Italy. Elected member of the Academic Senate, University of Padova, Italy. PhD in Mechanics of Structures. Coordinator of several research projects. Chairman of the RILEM "Technical Committee Design procedures for the use of composites in strengthening of Reinforced Concrete structures". Member of various International Technical Committees. Member of the Editorial Advisory Committee of the international journal of Materials and Structures. Keynote speaker and member of the Scientific Committee of various Conferences. Author of over 200 scientific publications.



**Gianluca Cusatis** is a faculty member of the Civil and Environmental Engineering Department at Northwestern University that he joined in August 2011. He teaches undergraduate and graduate courses of the civil engineering curriculum and performs research in the field of computational and applied mechanics, with emphasis on heterogeneous and quasi-brittle materials. His work on constitutive modeling of concrete through the adoption of the so-called Lattice Discrete Particle Model (LDPM), one of the most accurate and reliable approaches to simulate failure of materials experiencing strain-softening, is known worldwide. Under the sponsorship of several agencies including NSF, ERDC, and NRC his current research focuses on formulating and validating multiscale and multiphysics computational frameworks for the simulation of large scale problems dealing with a variety of different applications including, but not limited to, infrastructure aging and deterioration, structural resiliency, projectile penetration, and design of blast resistance structures. He is member of FraMCoS, ASCE, ACI, and USACM and active in several technical committees. He chairs the ACI 446 committee on Fracture Mechanics where he is leading an effort to develop practical guidelines for the calibration and validation of concrete models. He serves as treasurer for IA-FraMCoS.